Design and Practical Implementation of Multifrequency RF Front Ends Using Direct RF Sampling

Mark L. Psiaki, Steven P. Powell, *Member, IEEE*, Hee Jung, and Paul M. Kintner, *Senior Member, IEEE*

***Abstract*—The use of direct RF sampling has been explored as a means of designing multifrequency RF front ends. Such front ends will be useful to multifrequency RF applications such as global navigation satellite system receivers that use global positioning system (GPS) L1, L2, and L5 signals and Galileo signals. The design of a practical multifrequency direct RF sampling front end is dependent on having an analog-to-digital converter whose input bandwidth accommodates the highest carrier frequency and whose maximum sampling frequency is more than twice the cumulative bandwidth about the multiple carrier signals. The principle of direct RF sampling is used to alias all frequency bands of interest onto portions of the Nyquist bandwidth that do not overlap. This paper presents a new algorithm that finds the minimum sampling frequency that avoids overlap. This design approach requires a multifrequency bandpass filter for the frequency bands of interest. A prototype front end has been designed, built, and tested. It receives a GPS coarse/acquisition code at the L1 frequency and GPS antispoofing precision code at both L1 and L2. Dual-frequency signals with received carrier-to-noise ratios in excess of 52 dB-Hz have been acquired and tracked using this system.**

***Index Terms*—Analog–digital conversion, band-limited signals, global positioning system (GPS), radio receivers, sampled data systems, software radio.**

I. Introduction

DIRECT RF sampling is a radio receiver technique in which the RF signal of interest is sampled without first mixing the carrier signal down to a lower IF. The receiver can sample at a frequency that is much lower than the original carrier if the sampling frequency is more than twice the signal's information bandwidth and if appropriate bandpass pre-filtering is used. The sampled signal gets intentionally aliased down to an IF that is within the Nyquist bandwidth [1], [2].

A key enabling technology for an L-band receiver of this type is an analog-to-digital converter (ADC) that can process input signals in the 1–2-GHz range at continuous sampling frequencies in the 10–100-MHz range. Such technology is now available commercially.[1]

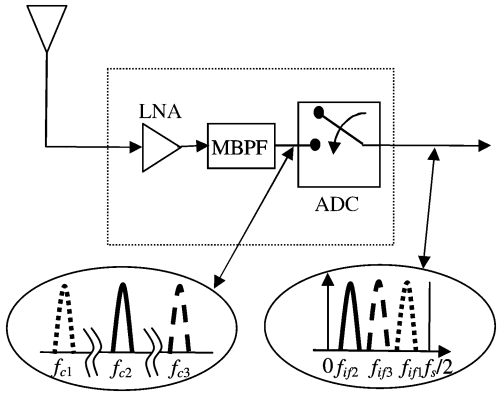

Fig. 1. Schematic block diagram of a multifrequency direct RF sampling receiver front end.

One advantage of direct RF sampling is the ability to process multiple frequency bands using a single front end. If the sampling frequency is chosen carefully, then multiple frequencies can be intentionally aliased to nonoverlapping portions of the Nyquist bandwidth, and a single output data stream will contain the signals from all frequency bands of interest [3]. This use of a single RF chain for all signals simplifies the front-end design, reduces the parts count, and eliminates numerous potential sources of differential line bias. A differential bias causes trouble when making multifrequency carrier-phase differential range measurements, as discussed in [4].

Fig. 1 illustrates the concept of a direct RF sampling front end that simultaneously receives multiple frequency bands. It consists of a low-noise amplifier (LNA), a multiband bandpass filter (MBPF), and an ADC with a sampler. The MBPF passes several frequency bands of interest and rejects all others. In this example, the frequency bands of interest are centered at the three widely separated carrier frequencies f_{c1}, f_{c2}, and f_{c3}. The ADC sampling frequency f_s is chosen so that it aliases each of the frequency bands to nonoverlapping portions of the Nyquist bandwidth from 0 to $f_s/2$, as depicted in the bubble associated with the ADC output. The aliased versions of the original carrier frequencies are f_{if1}, f_{if2}, and f_{if3}. Note how aliasing permutes their order.

Previous studies of direct RF sampling for a radio receiver front end include [1], [2], [3], and [5]. References [1] and [2]

Manuscript received January 18, 2005. This work was supported in part by the National Aeronautics and Space Administration Office of Space Science under Grant NAG5-12089 and Grant NAG5-12211.

M. L. Psiaki is with the Sibley School of Mechanical and Aerospace Engineering, Cornell University, Ithaca, NY 14853 USA (e-mail: mlp4@cornell.edu).

S. P. Powell and P. M. Kintner are with the School of Electrical and Computer Engineering, Cornell University, Ithaca, NY 14853 USA (e-mail: sp35@cornell.edu; pmk1@cornell.edu).

H. Jung was with the Sibley School of Mechanical and Aerospace Engineering, Cornell University, Ithaca, NY 14853-7501 USA. She is now with the Telecommunication Research and Development Center, Samsung Electronics Company Ltd., Suwon-City, Gyeonggi-Do, Korea 442-600 (e-mail: hj32.jung@samsung.com).

Digital Object Identifier 10.1109/TMTT.2005.855127

[1]MAX104. [Online]. Available: http://www.maxim-ic.com/quick_view2.cfm/qv_pk/2026, 2002.

concentrate on general aspects of direct RF sampling such as sensitivity and the effects of sampling jitter. References [3] and [5] deal specifically with multifrequency front-end design using direct RF sampling. Reference [5] concentrates on a design that uses a very high sampling frequency, i.e., 800 MHz, in order to capture the L1 and L2 global positioning system (GPS) bands. Aliasing does not alter the relationship between the two frequencies in this design, and the sampling frequency is much larger than the minimum required to capture the two 20-MHz code-division multiple-access (CDMA) code bandwidths at each carrier frequency. [3] develops constraints that determine the minimum required sampling frequency that is necessary to alias multiple passbands to nonoverlapping regions of the Nyquist bandwidth. It applies its approach to simultaneously acquire GPS L1 coarse/acquisition (C/A) signals and GLONASS signals using data from a single direct RF sampling front end. Reference [5] does not present experimental results.

This paper makes three contributions to the technology of direct RF sampling front ends for multifrequency signals. First, it develops an algorithm for calculating the minimum sampling frequency that aliases several bands of interest into the Nyquist bandwidth without allowing them to overlap. This contribution translates the constraints of [3] into a finite set of calculations that yield the optimal sampling frequency. Second, it presents the details of an actual RF front-end design that has been built to receive the GPS C/A code and precision code (P(Y)) on the L1 and L2 frequencies. Third, it presents actual dual-frequency acquisition and tracking results for signals that come out of this front end. These results demonstrate the sensitivity and accuracy of the dual-frequency direct RF sampling front end, and they explore the effects of discrete variations of the sampling frequency.

A preliminary version of this study is reported in [6]. The principal differences of this study are the addition of new 1-bit sampling results and a condensation of text.

The remainder of this paper consists of three main sections plus conclusions. Section II analyzes a multifrequency signal model. This leads to a criterion for the minimum sampling frequency that keeps the multiple frequency bands from overlapping after they get aliased into the Nyquist bandwidth. Section III describes the design of an actual dual-frequency direct RF sampling front end for the GPS L1 and L2 signals. Section IV presents experimental acquisition and tracking results for the system described in Section III. Section V summarizes this study and presents conclusions.

II. Modeling, Analysis, and Conceptual Design of a Multifrequency Direct RF Sampling Front End

The signal that exits the LNA of the RF front end can be modeled as

$$y(t) = \sum_{j=1}^{M} A_j(t)\cos\left[2\pi f_{cj}t + \phi_j(t)\right] + n(t). \qquad (1)$$

It contains M different frequency bands of interest with nominal carrier frequencies of f_{cj} for $j = 1, \ldots, M$. The envelop amplitude $A_j(t)$ and phase $\phi_j(t)$ for each band are baseband signals with bandwidth B_j. The term $n(t)$ models noise and interfering signals.

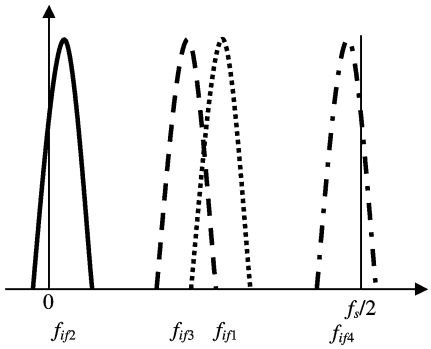

Fig. 2. Effects of a poor direct RF sampling frequency on signal overlap characteristics in the Nyquist bandwidth.

The RF front end's MBPF must be designed to leave each $A_j(t)$ and $\phi_j(t)$ largely unaffected, except for the addition of delay, while attenuating most of the out-of-band noise and interference contained in $n(t)$. Given such filtering, the sampled output of the ADC can be modeled as

$$y_l = \sum_{j=1}^{M} A_j(t_l)\cos\left[2\pi \bar{f}_{ifj}t_l + \phi_j(t_l)\right] + \nu_l \qquad (2)$$

where the subscript l refers to the sample time $t_l = l\Delta t_s = l/f_s$ with sample period Δt_s and sampling frequency $f_s = 1/\Delta t_s$. The sequence $\nu_0, \nu_1, \nu_2, \ldots, \nu_l, \ldots$ is discrete-time noise. The aliased intermediate equivalents of the original RF carrier frequencies are

$$\bar{f}_{ifj} = \bar{f}_{ifj}(f_s) = f_{cj} - f_s \text{round}\left(\frac{f_{cj}}{f_s}\right), \quad \text{for } j = 1, \ldots, M \qquad (3)$$

where the round() function rounds to the nearest integer. These IFs can fall anywhere from $-f_s/2$ to $+f_s/2$. Aliasing to a negative IF is analogous to high-side mixing. A positive version of the IF is $f_{ifj}(f_s) = |\bar{f}_{ifj}(f_s)|$.

An ideal direct RF sampling frequency will produce nonoverlapping aliased frequency bands, as shown in the lower right-hand-side bubble of Fig. 1 [3]. A poor choice of sampling frequency, on the other hand, might give rise to the aliased signal structure shown in Fig. 2. There are three bad aspects of this design: the frequency band centered at f_{if2} overlaps zero, the frequency bands centered at f_{if3} and f_{if1} overlap each other, and the frequency band centered at f_{if4} overlaps the aliasing frequency $f_s/2$.

The following constraints on f_s preclude situations like those depicted in Fig. 2 [3]:

$$a_j(f_s) = \frac{f_{ifj}(f_s)}{\frac{B_j}{2}} \geq 1, \qquad \text{for } j = 1, \ldots, M \qquad (4a)$$

$$b_j(f_s) = \frac{\frac{f_s}{2} - f_{ifj}(f_s)}{\frac{B_j}{2}} \geq 1, \qquad \text{for } j = 1, \ldots, M \qquad (4b)$$

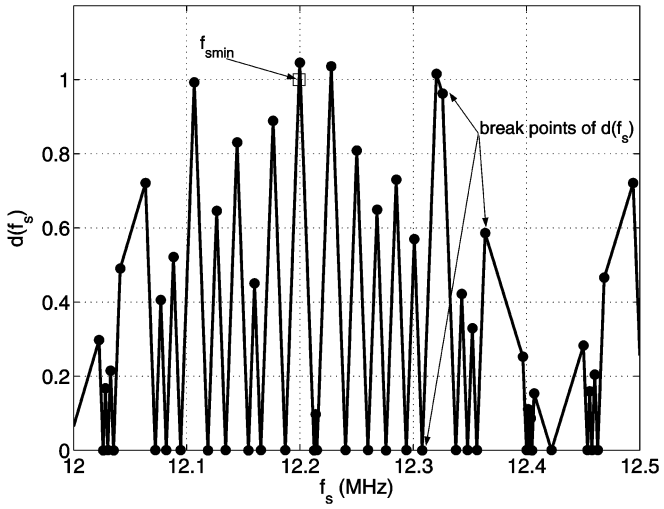

Fig. 3. Portion of the sampling frequency constraint function $d(f_s)$ for a civilian dual-frequency GPS front end.

$$c_{jk}(f_s) = \frac{|f_{ifj}(f_s) - f_{ifk}(f_s)|}{\frac{B_j}{2} + \frac{B_k}{2}} \geq 1, \quad \text{for } j = 1, \ldots, M-1; \quad k = (j+1), \ldots, M. \tag{4c}$$

Note that the constraint functions $a_j(f_s)$, $b_j(f_s)$, and $c_{jk}(f_s)$ are all guaranteed to be nonnegative.

These variant forms of the constraints of [3] can be used to define an explicit algorithm that determines sampling frequencies that satisfy them, including the minimum acceptable sampling frequency. The algorithm makes use of the following function:

$$d(f_s) = \min\big[a_1(f_s), \ldots, a_M(f_s), b_1(f_s), \ldots, b_M(f_s), c_{12}(f_s), c_{13}(f_s), \ldots, c_{M-1M}(f_s)\big]. \tag{5}$$

The set of acceptable sampling frequencies is $\{f_s : d(f_s) \geq 1\}$, and the minimum acceptable sampling frequency is the minimum positive value of f_s such that $d(f_s) \geq 1$.

The function $d(f_s)$ is piecewise linear. It can be fully characterized by the set of "break" points at which its slope changes and by the function's values at these break points. An example of this function is shown in Fig. 3. This example applies to a civilian dual-frequency GPS receiver. The input parameters to this function are $f_{c1} = 1575.42$ MHz, $f_{c2} = 1227.6$ MHz, $B_1 = 3.15$ MHz, and $B_2 = 2.46$ MHz. The break points of $d(f_s)$ are shown in the figure along with the minimum acceptable f_s value for this front end.

Given the break points f_{bi} and the corresponding function values $d(f_{bi})$, the acceptable f_s values can be calculated by considering each break point whose corresponding function value respects the limit $d(f_{bi}) \geq 1$. Given such a break point, a subset of the acceptable set is

$$\Big\{f_s : \big[(1-\lambda_{li})f_{bi-1} + \lambda_{li}f_{bi}\big] \leq f_s \leq \big[\lambda_{hi}f_{bi} + (1-\lambda_{hi})f_{bi+1}\big]\Big\} \tag{6}$$

where

$$\lambda_{li} = \begin{cases} \max\left[0, \dfrac{d(f_{bi-1})-1}{d(f_{bi-1})-d(f_{bi})}\right], & \text{if } d(f_{bi-1}) < d(f_{bi}) \\ 0, & \text{if } d(f_{bi-1}) \geq d(f_{bi}) \end{cases} \tag{7a}$$

$$\lambda_{hi} = \begin{cases} \max\left[0, \dfrac{d(f_{bi+1})-1}{d(f_{bi+1})-d(f_{bi})}\right], & \text{if } d(f_{bi+1}) < d(f_{bi}) \\ 0, & \text{if } d(f_{bi+1}) \geq d(f_{bi}). \end{cases} \tag{7b}$$

The set of acceptable sampling frequencies is the union of all sets as defined in (6) for all break points with $d(f_{bi}) \geq 1$. The minimum acceptable sampling frequency is $f_{smin} = [(1-\lambda_{li})f_{bi-1} + \lambda_{li}f_{bi}]$, where f_{bi} is the minimum break point that respects the limit $d(f_{bi}) \geq 1$.

The main difficulty in the calculation of acceptable f_s values is the calculation of the break points of $d(f_s)$. Once the f_{bi} values are known, it is straightforward to calculate the $d(f_{bi})$ values using (4a) and (5) and to calculate the set of acceptable f_s values and f_{smin} using (6) and (7b).

The set of break points can be determined in three steps. The first step recognizes that the IF functions $f_{ifj}(f_s)$ are piecewise linear and that their break points form a subset of the break points of $d(f_s)$ by virtue of (3) to (4b). The break points of $f_{ifj}(f_s)$ are $2f_{cj}/n$ for $n = 1, 2, 3, \ldots$. One need not consider an infinite number of n values because the break frequencies decrease as n increases, and it is known that $d(f_s) < 1$ for $f_s < 2(B_1 + \cdots + B_M)$. Therefore, one only needs to compute the break frequencies $2f_{cj}/n$ for $n = 1, 2, 3, \ldots, N_j$, where $N_j = \text{floor}[f_{cj}/(B_1 + \cdots + B_M)]$. The floor[] function rounds to the nearest integer in the direction of $-\infty$. The first step of the break frequency calculation assembles the set of all the break frequencies that are no lower than $2(B_1 + \cdots + B_M)$ for all the functions $f_{if1}(f_s), \ldots, f_{ifM}(f_s)$. It also sorts this set into ascending order.

The second step determines the additional break frequencies at which the functions $c_{jk}(f_s) = 0$. Each $c_{jk}(f_s)$ function is piecewise linear because of the piecewise linearity of the $f_{ifj}(f_s)$ functions and because of the piecewise linearity of the absolute value function. Its break frequencies consist of the already calculated break frequencies of the $f_{ifj}(f_s)$ and $f_{ifk}(f_s)$ functions coupled with the set of frequencies at which $f_{ifj}(f_s) = f_{ifk}(f_s)$. These new break frequencies can be calculated by considering each interval between elements of the union of the break frequencies of $f_{ifj}(f_s)$ and $f_{ifk}(f_s)$. Both $f_{ifj}(f_s)$ and $f_{ifk}(f_s)$ are linear on each such interval, and it is a matter of solving a scalar linear equation to determine whether they intersect in a given interval. If they do intersect, then the intersection frequency is added to the list of break frequencies. Each intersection is a break frequency of $d(f_s)$ because $c_{jk}(f_s) = 0$ at such a frequency, which implies that $d(f_s) = 0$. All of the linear intervals for all (j, k) combinations in the range $j = 1, \ldots, M-1$, $k = (j+1), \ldots, M$ must be considered in order to determine the complete set of $d(f_s)$ break frequencies that get added during this second step.

The third and last step determines additional break frequencies that are the frequencies at which the minimizing argument in (5) changes from one function to another. This step starts

with all of the break frequencies of the first two steps sorted into ascending order. It looks at each interval between pairs of adjacent break frequencies from the first two steps. In each of these intervals, each of the functions $a_1(f_s),\ldots,a_M(f_s)$, $b_1(f_s),\ldots,b_M(f_s)$, $c_{12}(f_s),c_{13}(f_s),\ldots,c_{M-1M}(f_s)$ are linear. The intersection frequency for each pair of functions in this set gets calculated by solving a scalar linear equation. If this frequency falls within the interval in question and if the two functions are less than all of the other functions at this frequency, then this frequency is an additional break frequency of $d(f_s)$. All intersections are considered for all function pairs and for all frequency intervals from the first two steps. The set of all minimizing intersection frequencies gives the entire set of break frequencies at which $d(f_s) \neq 0$. These correspond to the black dots with $d(f_s) > 0$ in Fig. 3, and the $d(f_s) = 0$ dots correspond to break frequencies from the first two steps. This new set of frequencies gets combined with the frequencies from the first two steps to yield the full set of $d(f_s)$ break points.

Although complicated, these offline design calculations execute relatively quickly. Only 1653 $d(f_s)$ break points had to be calculated for the design associated with Fig. 3.

III. Hardware Design of an Example Dual-Frequency Direct RF Sampling Front End

A. Sampling Frequencies

A dual-frequency direct RF sampling front end has been designed and built. Its function is to receive the GPS C/A and P(Y) codes on L1 and the P(Y) code on L2. Its outputs are used in an offline software receiver that does optimal semicodeless acquisition and tracking of the P(Y) code on L2 while simultaneously tracking the C/A code on L1 [7].

The techniques of Section II have been employed to design suitable sampling frequencies. Three trial frequency designs have been developed, i.e., $f_s = 55.5053$ MHz, 77.33 MHz, and 99.23 MHz. The lowest of these sampling frequencies allows some overlap of the 10.23-MHz P(Y) codes' CDMA power spectrum main lobes; half the separation between the two aliased carrier frequencies is only 7.39 MHz, and their separations from 0 or $f_s/2$ are only 6.48 MHz. The advantage of this lower frequency is a reduced computational load downstream of the front end. The sampling frequency 77.33 MHz reduces the overlaps significantly. The 99.23-MHz sampling frequency completely separates the main lobes; the aliased carrier frequencies differ from 0 and $f_s/2$ by at least 12.26 MHz and from each other by twice 12.29 MHz.

B. Functional Block Diagram and Explanation of Component Interactions

The experimental dual-frequency direct RF sampling front end is shown in block-diagram form in Fig. 4 and photographically in Fig. 5. The RF front end consists of the elements that are contained in the irregularly shaped dashed–dotted contour that occupies most of the right-hand side of Fig. 4. The first part of the front end is an attenuator that allows adjustment of the power level at the eventual input to the ADC. Next comes an active dual-frequency filter assembly that includes two dual-frequency bandpass filters, labeled MBPF1 and MBPF2, with an

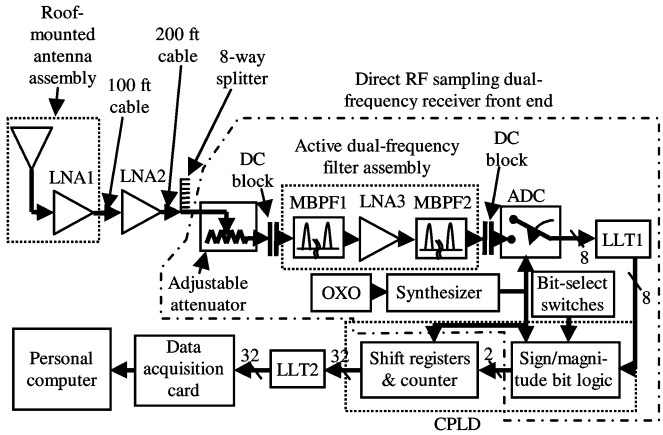

Fig. 4. Block diagram of GPS L1/L2 dual-frequency direct RF sampling front end and associated experimental hardware.

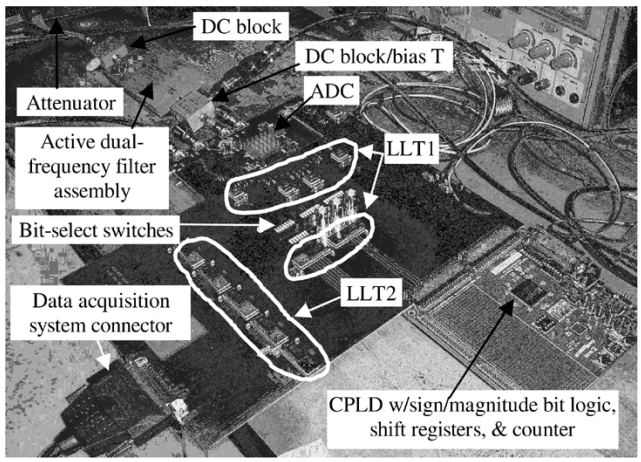

Fig. 5. Prototype GPS L1/L2 dual-frequency direct RF sampling front end.

LNA in between, labeled LNA3. The ADC is just down stream of this filter assembly. Its eight output bits go through a logic level transformer (LLT1) and into a sign/magnitude bit logic unit that is part of a complex programmable logic device (CPLD). LLT1 transforms from the ADC's differential logic levels to those of the CPLD. The sign/magnitude block performs simple logic operations on the ADC's sign bit and a user-selectable pair of its seven magnitude bits and produces the RF front end's two output bits, a magnitude bit, and a sign bit.

The reduction from eight to two bits distinguishes this RF front end from the one used in [3], which recorded all four bits of its ADC output. The ability to use fewer bits without significant loss of carrier-to-noise ratio is important for multifrequency direct RF sampling systems because of the high sampling rates involved. A reduction in the number of output bits reduces the required memory and digital processing downstream of the front end.

The RF front end includes an ovenized crystal oscillator (OXO) and a frequency synthesizer, which are used to generate the sample clock for the ADC. The sample clock signal also drives the sign/magnitude bit logic and a shift register system.

The other equipment shown in Fig. 4's block diagram is used to experimentally evaluate the RF front end. This equipment includes a dual-frequency GPS patch antenna, two LNAs, two

long cable runs, and a splitter, all of which are upstream of the RF front end. These are used to receive signals from actual satellites and transmit them from the roof of a building into a laboratory. The shift-register/counter circuit that is immediately downstream of the RF front end deserializes the sign and magnitude output bit streams. It creates 32-bit words that get read into the computer by the data acquisition card once every 16 samples. The LLT2 block between the shift registers and the data acquisition system translates the CPLD's logic levels to those of the data acquisition system. The personal computer stores the input data on disk and processes it offline using software receiver code that runs in MATLAB.

C. Gain Control

The adjustable attenuator gets used in order to perform "human-in-the-loop" gain control. Coarse adjustment, along with proper design of the other upstream elements ensures that the signal power at the input to the ADC is within its allowable operating range. Fine adjustment seeks to minimize the carrier-to-noise ratio's digitization loss [8]. The optimal gain yields a certain percentage of samples that produce a high magnitude bit.

Digital automatic gain control logic can be added to the sign/magnitude bit logic unit. Digital gain control considers all seven magnitude bits and uses feedback to automatically adjust the digital threshold for the high magnitude output bit. Such a system can have a gain adjustment range of almost $(2^7)^2$ or 42 dB.

D. Descriptions of Significant Parts

Short descriptions of the actual models that have been used for the five most significant or unusual components of the system are presented here. The active dual-frequency filter assembly is a Delta Microwave model L5658 low-noise GPS filter/amplifier. Its passbands are centered at 1575.4 and 1227.6 MHz, and each has a 1-dB two-sided bandwidth of at least 20 MHz. It has a gain of 43 dB and a maximum noise figure of 2.7 dB. The two passbands' maximum gains are within 2 dB of each other, with the gain at L1 being the lower of the two.

The ADC is model MAX104 made by Dallas Semiconductor MAXIM, Dallas, TX. It can process input signals with bandwidths up to 2.2 GHz and can sample continuously at sampling frequencies up to 1 GHz. It has eight bits of output, and the maximum input power level is 0.625 mW (250 mV 0-to-peak at 50 Ω). Its aperture jitter is less than 0.5 ps.

Given that only two bits of the ADC data are retained, it should be possible to implement an RF front end using a simpler ADC. This could lower the cost and power consumption of the system (the MAX104 consumes approximately five watts). A 2-bit ADC should give equivalent performance, but this would require implementation of an analog automatic gain control system. A 1-bit ADC would be simpler and would not require an automatic gain controller, but sensitivity would decrease by 1.5–2.3 dB [8].

The CPLD is manufactured by XILINX, San Jose, CA. The chip is model number XC2C256 and is mounted on the XC2 board. It can operate at clock frequencies in excess of 100 MHz. Its programmable gates can be used to implement Boolean logic, shift registers, and counters. The current application makes use of less than 32% of its 256 available macrocells.

The OXO is a model 1811AAAB high-stability OCXO made by CTS Reeves, Bloomingdale, IL. It has a 10-MHz nominal frequency. It has an rms phase noise of less than 1.2×10^{-6} cycles. Studies indicate that the system can function satisfactorily using only a temperature-compensated crystal oscillator [2], but an ovenized oscillator has been used in the prototype system as a means of reducing design uncertainty.

Two different frequency synthesizers have been used to generate the ADC sample clock signal from the OXO's 10-MHz reference signal. One is a FLUKE model 6060B synthesized RF signal generator. The other is an HP model 3325A synthesizer/function generator. The FLUKE synthesizer can go up to 1050 MHz, while the HP synthesizer is limited to frequencies below 61 MHz. The FLUKE synthesizer's rms phase noise can be as high as 2×10^{-3} cycles for the 55–100-MHz ADC sampling frequency range of interest. The HP synthesizer's maximum rms phase noise is more than one order of magnitude smaller, less than 2×10^{-4} cycles. The high phase noise of the FLUKE synthesizer can cause the received signal to exhibit significant carrier phase jitter when sampling in the frequency range of interest [2], but useful results can be achieved despite this shortcoming.

The other components in the experimental setup yield a typical overall noise figure of 1.0 dB and a gain of 95 dB upstream of the ADC. The noise figure is set primarily by LNA1. This represents a reasonably sensitive system. Nonlinear distortion is not significant in this system because the GPS signal power and the noise power are much smaller than the 1-dB compression point and the third-order intermodulation intercept point of the cascaded inline amplifiers.

IV. Performance Evaluation Based on Experimental Data

The performance of the prototype dual-frequency direct RF sampling GPS receiver front end has been evaluated using several sets of experimental data. The L1 C/A code has been acquired and tracked. The C/A navigation data bit changes have been used to remove the 180° carrier phase ambiguity and to achieve GPS data frame lock. The frame lock information and the carrier phase information from the L1 C/A code have been used to generate the quadrature baseband signal on L1 and to correlate this signal with a Precision (P) code replica. The alignment of the P code with the C/A code on L1 has been verified using semicodeless techniques [9]. The L1 results have been used to perform semicodeless acquisition and tracking of the P(Y) code on L2. In addition, signal amplitudes, carrier-to-noise ratios, and power spectral densities have been examined.

A. Reception of GPS C/A and P(Y) Codes on L1

Consider a typical case that illustrates the performance of the new front end. Thirty-two seconds worth of data have been recorded at approximately 22 : 00 UT on 27 February 2003 using $f_s = 99.23$ MHz from the FLUKE synthesizer. The GPS L1 C/A signal for PRN code 24 has been acquired and tracked. This is one of the strongest signals present in the data. Its received C/A carrier-to-noise ratio is $C/N_0 = 54.6$ dB-Hz.

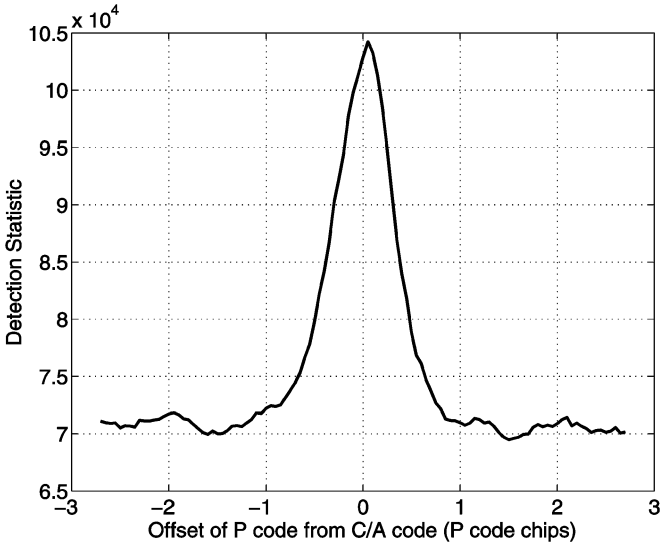

Fig. 6. Semicodeless acquisition statistic for the GPS P(Y) code on L1 as a function of the P code replica's time offset from the tracked C/A code.

This is a strong C/N_0 for a patch antenna. Typical maximum C/N_0 values on the order of 50–51 dB-Hz have been observed for the GPS L1 C/A signal when using a patch antenna and a commercial 2-bit RF front end that employs automatic gain control (Zarlink/Plessey GP2015). Thus, the new front end has good sensitivity for GPS C/A signals on L1.

The GPS P(Y) code acquisition on L1 has used semicodeless techniques similar to those described in [9]–[12]. Fig. 6 plots the P(Y) code's semicodeless detection statistic as a function of its offset from the C/A code. It is clear from this figure that the front end successfully receives the L1 P(Y) code and that the P(Y) code is offset from the C/A code by no more than 1/20th of a P-code chip.

B. Semicodeless Acquisition and Tracking of GPS P(Y) Code on L2

The efficacy of the prototype dual-frequency RF front end for GPS L2 reception has been demonstrated by using semicodeless techniques to acquire and track the L2 P(Y) signal, as described in [7] and [9]. Fig. 7 shows the results of semicodeless acquisition of P(Y) on L2 for PRN code 24 using the 27 February 2003 data set that samples at $f_s = 99.23$ MHz. The detection statistic is plotted as a function of the L1/L2 delay. The L2 P(Y) code lags L1 by approximately 0.24 P code chips, or 23 ns, which represents a reasonable level of ionospheric delay.

The L2 signal has also been tracked for this case. The Kalman-filter-based optimal tracking techniques of [7] have been used to track the L2 code phase, carrier phase, carrier Doppler shift, and rate-of-change of carrier Doppler shift. These quantities can be compared with the corresponding L1 values to check whether they are reasonable. As an example, consider Fig. 8, which plots two line-of-sight (LOS) velocity time histories for the GPS satellite that broadcasts PRN code 24. The dashed–dotted grey curve shows the LOS velocity as estimated from the C/A carrier tracking loop on L1, and the solid black curve is based on the semicodeless P(Y) carrier tracking on L2. The two curves fall right on top of each other,

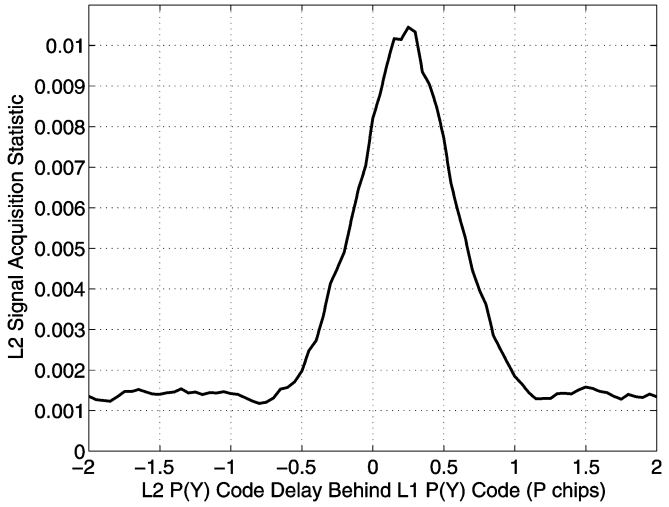

Fig. 7. Semicodeless acquisition statistic for the GPS P(Y) code on L2 as a function of the offset from the P(Y) code on L1.

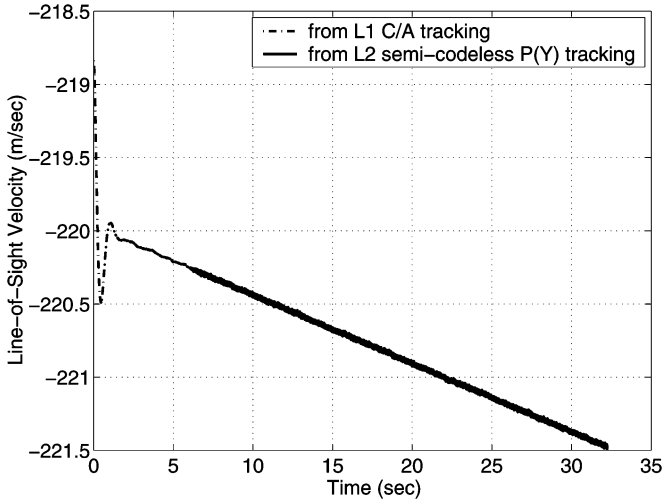

Fig. 8. Estimated LOS velocity from GPS L1 C/A carrier tracking and from GPS L2 P(Y) semicodeless carrier tracking.

which confirms that the new prototype dual-frequency RF front end receives both the L1 and L2 bands with reasonable sensitivity and without any frequency bias. The increased noisiness of the L2 LOS velocity as compared to the L1 velocity is partly the result of the poorer processing gain of the semicodeless tracking technique and partly the result of sub-optimal tuning of the L2 tracking algorithm.

C. Relative Signal Amplitudes and the Received Power Spectral Density

The code and carrier tracking algorithms of [7] also estimate signal amplitudes. These results allow one to consider the relative amplitudes of the various codes. PRN code 24 exhibits a P(Y) power on L1 that is 4 dB lower than the L1 C/A power for the 27 February 2003 data set with $f_s = 99.23$ MHz. This is consistent, to within experimental error, with the nominal 3-dB difference that is supposed to exist between the two power levels [13].

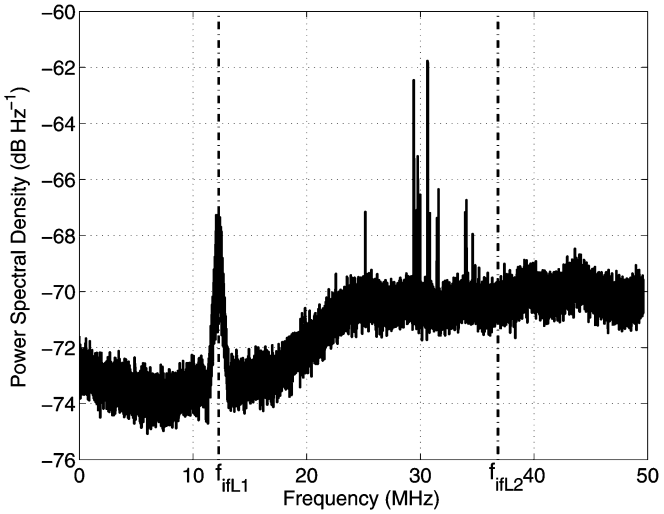

Fig. 9. Power spectrum of the output of the prototype GPS L1/L2 dual-frequency direct RF sampling front end when $f_s = 99.23$ MHz.

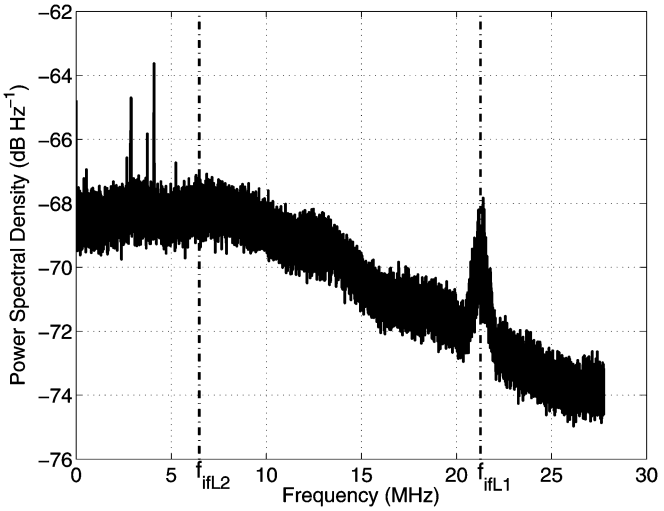

Fig. 10. Power spectrum of the output of the prototype GPS L1/L2 dual-frequency direct RF sampling front end when $f_s = 55.5053$ MHz.

Another interesting power comparison is between the P(Y) code on L1 and the P(Y) code on L2. The latter is 1.6 dB stronger than the former for PRN code 24 in the 27 February 2003 data set. The nominal L2 P(Y) power is supposed to be 3 dB weaker than the L1 P(Y) power [13]. What can account for this 4.6-dB discrepancy from the nominal relationship?

Much of the answer lies in the characteristics of the dual-frequency RF front end. Fig. 9 shows the power spectrum of the output of the front end when sampling at 99.23 MHz. The aliased intermediate values of the L1 and L2 carrier frequencies f_{ifL1} and f_{ifL2} are marked on Fig. 9 as vertical dashed–dotted grey lines. The power spectrum clearly shows a 2-MHz-wide peak at f_{ifL1}, which corresponds to the C/A codes of the satellites in view. It also shows a noise floor that is 3 dB higher near L2 than near L1. This difference is probably caused by differential amplification of the L1 and L2 signals in the RF chain that is upstream of the front end's ADC. Measurements of the active dual-frequency filter assembly indicate that it may contribute as much as 2 dB of this difference.

The apparent difference of amplification can account for 3 dB of the 4.6-dB amplitude ratio discrepancy between the P(Y) code on L1 and the P(Y) code on L2. Two possible contributing factors to the remaining 1.6-dB discrepancy are off-nominal operation of PRN code 24 and a narrower MBPF bandwidth for L1 in comparison to L2.

The received carrier-to-noise ratios of the P(Y) codes on L1 and L2 are, respectively, $(C/N_0)_{\mathrm{L1}} = 53.8$ dB-Hz and $(C/N_0)_{\mathrm{L2}} = 52.3$ dB-Hz. These are reasonably high levels, which indicates good sensitivity of the prototype RF front end. It is interesting to note that C/N_0 of the P(Y) code on L1 is only 0.8 dB weaker than C/N_0 of the C/A code even though the signal is 4 dB weaker. This fact results from the different noise sources for the two signals. Fig. 9 shows that the cumulative power spectral density of the C/A codes on L1 are approximately 3–4 dB above the noise floor. Thus, the primary noise source for a given C/A code is not thermal noise. Instead, it is interference from the other C/A codes.

Fig. 9 shows two other interesting features. One is the rolloff of the L2 filter, which can be seen as a noise power change over the frequency range from 18 to 23 MHz. The other is the presence of narrow noise spikes between 25–34 MHz. Analysis of the power spectral density plots that result when using the different sampling frequencies $f_s = 55.5053$ MHz and 77.33 MHz indicate that these spikes are actual interfering RF signals centered at approximately 1558 MHz.

D. Performance With a 1-bit ADC

The performance of this system has been examined when only 1 bit of ADC data is used. The retained bit is the sign bit. Such a system does not require gain control and can use an ADC that is less complex, lower in cost, and less power hungry. The performance of a 1-bit system has been investigated using experimental data from the example implementation running at the sampling frequency $f_s = 99.23$ MHz. The 1-bit performance is similar to that of the 2-bit system. The only noticeable difference is an expected slight degradation of C/N_0. The C/A code on L1 and the P(Y) code on L2 both lose approximately 1 dB, while the P(Y) code on L1 experiences a 2-dB loss. These losses are consistent with the theoretically expected loss range of 1.5–2.3 dB [8].

E. Operation at Other Sampling Frequencies

The performance of the dual-frequency front end has been investigated at the two additional sampling frequencies that are mentioned at the beginning of Section III, i.e., $f_s = 55.5053$ MHz and 77.33 MHz. The primary effect of using one of these lower sampling frequencies is an increase in the noise density. Fig. 10 shows the power spectrum of the output of the RF front end for data that has been taken on 11 July 2003 using $f_s = 55.5053$ MHz. Compare this to the power spectral density of Fig. 9, which corresponds to $f_s = 99.23$ MHz. Fig. 10 shows a noise density at f_{ifL1} that is approximately 1 dB higher than the corresponding noise density in Fig. 9, and its noise density at f_{ifL2} is approximately 2 dB higher than in Fig. 9. One expects the average noise density in Fig. 10 to be larger by approximately $10\log_{10}(99.23/55.5053) = 2.5$ dB; thus, the actual increases are not as large as one might expect.

The higher noise density comes about because out-of-band noise gets aliased into the Nyquist bandwidth and because noise from the two different frequency bands starts to overlap.

V. Summary and Conclusions

Direct RF sampling has been explored as a means of designing multifrequency RF front ends for radio receivers. These front ends use specially designed sampling frequencies that alias the frequency bands of interest onto nonoverlapping portions of the Nyquist bandwidth. A multifrequency bandpass filter upstream of the ADC prevents unwanted out-of-band signals and noise from getting aliased on top of the signals of interest. The ADC must have an allowable input bandwidth that is higher than the highest RF frequency of interest. A mathematical algorithm has been developed for the selection of sampling frequencies, and a prototype dual-frequency system has been built and tested. The prototype system receives the GPS C/A code on the L1 frequency band and the GPS P(Y) code on the L1 and L2 bands.

The prototype receiver front end has been tested at several sampling frequencies. It has been used to successfully acquire and track GPS C/A code on L1 and GPS P(Y) code on L1 and L2. One version of the front end outputs a 2-bit digitized signal and uses gain control to achieve good sensitivity; another version outputs a 1-bit signal. The strongest received GPS C/A signals from a roof-mounted dual-frequency antenna have carrier-to-noise ratios in excess of 54 dB-Hz, and the strongest received GPS P(Y) code signals have carrier-to-noise ratios between 51–54 dB-Hz.

References

[1] D. M. Akos and J. B. Y. Tsui, "Design and implementation of a direct digitization GPS receiver front end," *IEEE Trans. Microw. Theory Tech.*, vol. 44, no. 12, pp. 2334–2339, Dec. 1996.

[2] M. L. Psiaki, D. Akos, and J. Thor, "A comparison of 'direct RF sampling' and 'down-convert & sampling' GNSS receiver architectures," in *Proc. 16th Int. Satellite Division of the Institute of Navigation Tech. Meeting*, 2003, pp. 1941–1952.

[3] D. M. Akos, M. Stockmaster, J. B. Y. Tsui, and J. Caschera, "Direct bandpass sampling of multiple distinct RF signals," *IEEE Trans. Commun.*, vol. 47, no. 7, pp. 983–988, Jul. 1999.

[4] C. Goad, "Surveying with the global positioning system," in *Global Positioning System: Theory and Applications*, B. W. Parkinson and J. J. Spilker, Jr., Eds. Reston, VA: AIAA, 1996, vol. 2, pp. 501–517.

[5] A. Brown and B. Wolt, "Digital L-band receiver architecture with direct RF sampling," in *Proc. IEEE Position, Location, Navigation Symp.*, 1994, pp. 209–216.

[6] M. L. Psiaki, S. P. Powell, H. Jung, and P. M. Kintner, Jr., "Design and practical implementation of multi-frequency RF front ends using direct RF sampling," in *Proc. 16th Int. Satellite Division of the Institute of Navigation Tech. Meeting* , 2003, pp. 90–102.

[7] H. Jung, M. L. Psiaki, and S. P. Powell, "Kalman-filter-based semi-codeless tracking of weak dual-frequency GPS signals," in *Proc. 16th Int. Satellite Division of the Institute of Navigation Tech. Meeting*, 2003, pp. 2515–2523.

[8] A. J. Van Dierendonck, "GPS receivers," in *Global Positioning System: Theory and Applications*, B. W. Parkinson and J. J. Spilker, Jr., Eds. Reston, VA: AIAA, 1996, vol. I, pp. 329–407.

[9] K. T. Woo, "Optimum semicodeless carrier-phase tracking of L2," *Navigation*, vol. 47, pp. 82–99, Summer 2000.

[10] R. G. Keegan, "P-code-aided global positioning system receiver," U.S. Patent 4 972 431, Nov. 20, 1990.

[11] R. G. Lorenz, R. J. Helkey, and K. K. Abadi, "Global positioning system receiver digital processing technique," U.S. Patent 5 134 407, Jul. 28, 1992.

[12] R. K. T. Woo, J. O. Quan, and U. Cheng, "System and method for demodulating global positioning system signals," U.S. Patent 6 125 135, Sep. 26, 2000.

[13] J. J. Spilker, Jr., "GPS signal structure and theoretical performance," in *Global Positioning System: Theory and Applications*, B. W. Parkinson and J. J. Spilker, Jr., Eds. Reston, VA: AIAA, 1996, vol. I, pp. 57–119.

Mark L. Psiaki received the B.A. degree in physics and M.A. and Ph.D. degrees in mechanical and aerospace engineering from Princeton University, Princeton, NJ, in 1979, 1984, and 1987, respectively.

Since 1986, he has been a faculty member with the Sibley School of Mechanical and Aerospace Engineering, Cornell University, Ithaca, NY, where he has served as an Acting Assistant Professor (1986–1987), an Assistant Professor (1987–1993), and an Associate Professor (1993-present). From 1994 to 1995 and in 2001, he was a Visiting Associate Professor of aerospace engineering with the Technion, Haifa, Israel. His research interests are in the areas of estimation and filtering, GPS technology and applications, and spacecraft attitude and orbit determination.

Steven P. Powell (M'79) received the B.S. and M.S. degrees in electrical engineering from Cornell University, Ithaca, NY, in 1982 and 1983, respectively.

From 1983 to 1984, he was a Staff Engineer II with the School of Electrical Engineering, Cornell University. In 1984, he was a Member of the Technical Staff with the Recon Division, Watkins-Johnson Company, San Jose, CA. Since 1985, he has been a Senior Engineer with the Space Plasma Physics Group, School of Electrical and Computer Engineering, Cornell University. He has been involved with the design, fabrication, and testing of several GPS receivers. He has also participated in the design, fabrication, testing, and launch activities of numerous scientific experiments flown on high-altitude balloons, sounding rockets, and small satellites.

Hee Jung received the B.S. and M.S. degrees in astronomy from Seoul National University, Seoul, Korea, in 1992 and 1994, respectively, the M.S. degree in aerospace engineering from Texas A&M University, College Station, in 1999, and is currently working toward the Ph.D. degree in mechanical and aerospace engineering at Cornell University, Ithaca, NY.

Since 2004, she has been a Senior Engineer with the Telecommunication Research and Development Center, Samsung Electronics Company Ltd., Suwon-City, Gyeonggi-Do, Korea. Her main research interests are GPS receivers and applications and satellite orbit and attitude determination.

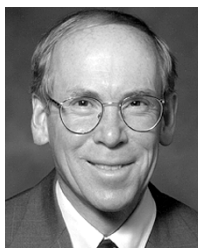

Paul M. Kintner (SM'82) received the B.S. degree in physics from the University of Rochester, Rochester, NY, in 1968, and the Ph.D. degree in physics from the University of Minnesota at Minneapolis, in 1974.

From 1974 to 1976, he was a Research Associate with the Department of Physics and Astronomy, University of Iowa. Since 1976, he has been with the School of Electrical and Computer Engineering, Cornell University, Ithaca, NY, where he has been a Research Associate (1976–1978), a Senior Research Associate and Lecturer (1978–1981), an Assistant Professor (1981–1985), an Associate Professor (1985–1991), and a Professor (1991-present). His research is in space physics and engineering with a specific interest in ionospheric effects on GPS and using GPS to remotely sense the ionosphere.